Chapter 8

Testing the Neupert Effect With the Combined Fokker-Planck and Hydrodynamic Codes

8.1 Energy Budget and the Neupert Effect

As shown in Chapter 6 (also Liu, W. et al., 2006), a simple test of the Neupert effect does not yield a better correlation between the SXR derivative and the electron power than that between the former and the HXR flux. This is not expected to be the case, but it is not surprising either because of nonlinearity involved in the energy redistribution and radiation processes. To further understand this question, one needs to check the energy budget and calculate HXR and SXR radiation properly. Veronig et al. (2005) investigated the Neupert effect using *RHESSI* observations and reached similar conclusion as we did. However, they calculated the various energy contents in an approximate way. The combined HD and particle calculation we have done here can help shed light on this question more quantitatively.

In general, the total energy $U(t)$ in the plasma consists of thermal energy $U_{\rm th}(t)$, kinetic energy $U_k(t)$, and gravitational energy $U_g(t)$.

$$U(t) = U_{\rm th}(t) + U_k(t) + U_g(t), \tag{8.1}$$

which can be readily calculated (integrating over the loop volume) from the distribution of density ρ (or n_e and n_i), temperature T, velocity v. For example,

$$U_{\rm th} = \int \frac{P}{\gamma - 1} dV = \int 3 n_e k T dV, \tag{8.2}$$

for $\gamma = 5/3$, and $n_e = n_i$. We set the reference level (zero height) of the gravitational potential at the bottom boundary (about 4 Mm below the transition region) and this gives the the value of U_g about 1/3 of the total energy in the initial state ($t = 0$). We find in all of our simulations that the temporal variation rate of the gravitational energy only constitutes about 1% of that of the total energy and thus is unimportant in the energy budget (and

not shown in our discussion below). The time derivative of these energies,

$$\dot{U}(t) = \dot{U}_{\rm th}(t) + \dot{U}_k(t) + \dot{U}_g(t), \tag{8.3}$$

gives the net energy gain of the system and should be balanced by the energy input (by electrons) rate $\dot{\mathcal{E}}_e$ and the energy loss rate L, namely,

$$\dot{U} = \dot{\mathcal{E}}_e - L\,. \tag{8.4}$$

The total energy loss rate generally has two components, radiative loss ($L_{\rm rad}$) and conductive loss ($L_{\rm cond}$) from the loop volume. In this particular study, the conduction flux vanishes at both the top and bottom boundaries, where we set the symmetric boundary condition and fix the temperature at $T = 10^4\,{\rm K}$, respectively, both giving rise to $\nabla T = 0$. Therefore, the only energy loss channel is through radiation (UV and optical),

$$L = L_{\rm rad} + L_{\rm cond}\,;\;\; L_{\rm cond} = 0 \implies L = L_{\rm rad}\,. \tag{8.5}$$

Thermal bremsstrahlung radiation at photon energy ϵ produced by a single temperature (i.e., Maxwellian distribution) plasma can be calculated via (Cox 2000, p. 184; Tandberg-Hanssen & Emslie 1988 p. 114):

$$I_{\rm SXR} = D({\rm EM})\frac{\exp(-\epsilon/kT)}{\epsilon\sqrt{T}}g(\epsilon/kT), \tag{8.6}$$

in which

$$D = (8/\pi m_e k)^{1/2}\,\kappa_{BH} Z^2 = 5.7\times10^{-12} Z^2 (\,{\rm cm^3\,s^{-1}\,K^{1/2}}),$$

where Z is the mean ionic charge which equals unity in our model and $\kappa_{BH} = (8\alpha/3) r_0^2 m_e c^2 = 7.9\times10^{-25}\,{\rm cm^2\,keV}$ is the constant in the Bethe-Heitler bremsstrahlung cross-section ($\alpha = 1/137$), ${\rm EM} = \int n_e n_i dV = \int n_e^2 dV$ is the emission measure (assuming $n_e = n_i$), $g(\epsilon/kT) = (kT/\epsilon)^{2/5}$ is the Gaunt factor (valid for temperature range $T > 7\times10^5\,{\rm K}$, Li et al. 1993). Substituting these quantities into equation (8.6), we have

$$I_{\rm SXR} = \frac{5.7\times10^{-12}}{\epsilon\sqrt{T}}\exp\left(-\frac{\epsilon}{kT}\right)\left(\frac{kT}{\epsilon}\right)^{2/5}\int n_e^2 dV \quad ({\rm photons\,s^{-1}\,keV^{-1}}), \tag{8.7}$$

where ϵ is in keV, T in K, and n_e in ${\rm cm^{-3}}$. In contrast to $U_{\rm th}$, $I_{\rm SXR}$ depends on n_e and T nonlinearly. In addition, $I_{\rm SXR}$ is not a monotonic function of T (see Fig. 8.1). Differentiating equation (8.7) gives the temperature where the maximum of $I_{\rm SXR}$ is located,

$$\frac{\partial I_{\rm SXR}}{\partial T} = \frac{I_{\rm SXR}}{T}\left(\frac{\epsilon}{kT} - \frac{1}{10}\right) \implies T_{\rm max} = 10\epsilon/k, \tag{8.8}$$

below (above) which $I_{\rm SXR}$ increases (decreases) monotonically with T. In other words, when a plasma is overheated and its temperature exceeds $10\epsilon/k$, its thermal radiation will decrease with increasing temperature[1]. This introduces more nonlinearity into the

[1]However, the total bremsstrahlung radiation increases as $\sqrt{T}$.

dependence of $I_{\rm SXR}$ on T. In the low temperature range, $T < T_{\rm max}$, however, a positive correlation (not necessarily linear though) between the thermal bremsstrahlung radiation $I_{\rm SXR}$ and the thermal energy $U_{\rm th}$ is expected. Or equivalently, their time derivatives, $\dot{I}_{\rm SXR}$ and $\dot{U}_{\rm th}$, would also exhibit a similar correlation.

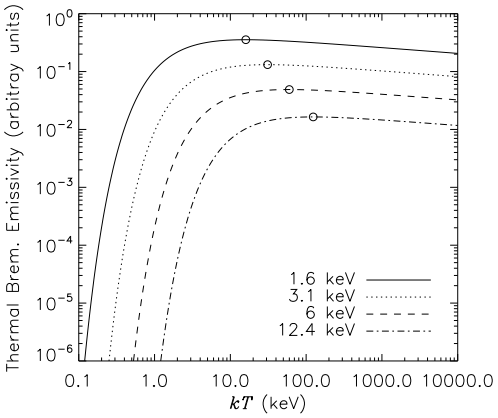

Figure 8.1: Thermal bremsstrahlung emissivity as a function of plasma temperature at different photon energies: $\epsilon = 1.6$, 3.1, 6, 12.4 keV. The open circles mark the maxima of these curves at the corresponding temperature of $T_{\rm max} = 10\epsilon/k$.

The *GOES* low channel (1–8 Å , 1.6–12.4 keV) flux is usually used as the SXR emission in Neupert effect studies. As long as $kT < 16\,{\rm keV}$ (which is usually the case for solar flares) the condition of $kT < 10\epsilon$ is satisfied in the entire 1–8 Å channel, so that $I_{\rm SXR}$ is an increasing function of T and we expect a positive $\dot{I}_{\rm SXR}$–$\dot{U}_{\rm th}$ correlation. To check if such an correlation is present in our five simulation cases we calculate, as shown in the following subsections, the thermal bremsstrahlung emission at $\epsilon = 1.6\,{\rm keV}$ [2] and $\epsilon = 6\,{\rm keV}$, which are at the low energy end and near the middle of the 1–8 Å channel, respectively.

8.2 Case R: Reference Calculation

8.2.1 History of Energy Budget

Let us check the **energy budget history** of Case R, which is shown in Figure 8.2. The total energy, thermal energy, and kinetic energy integrated over the whole loop are plotted in panel *a*; their time derivatives together with the electron energy deposition power $\dot{\mathcal{E}}_e$ and radiative loss rate $L_{\rm rad}$ are shown in panel *b*. As is evident, early on ($t \lesssim 15\,{\rm s}$) most of the energy deposited by electrons is quickly radiated away. This is because the coronal density is low at this time and the electron energy deposition is concentrated in the upper

[2]Note that continuum emission dominates over line emission in the *GOES* 1–8 Å channel (Culhane & Acton, 1970) and thus thermal free-free emission at a photon energy of 1.6 keV would be a good protocol for the *GOES* 1–8 Å flux. We take the low energy end (1.6 keV) because of the exponential decay (with photon energy) of thermal free-free emission. However, if one attempts to make a direct comparison with *GOES* observations, line emission must be calculated, say, using the current Chianti code, and then be added to the continuum and integrated over the entire 1–8 Å range, which is beyond the scope of this study.

chromosphere where radiative loss is the highest (see Fig. 7.3). As a result, only a small fraction of electron energy is available to heat the plasma and produces a slow increase of the total energy (Fig. 8.2*b*). However, as the flare evolves and chromospheric evaporation takes place, the coronal density increases and more electron energy is deposited above the transition region. This part of energy in turn heats and evaporates plasma more efficiently than in the upper chromosphere. Therefore, the radiative loss rate gradually drops and its competitor, electron energy deposition, takes over the control of the energy budget. This effect is present in Figure 8.2*b* as the rapid rise of the total energy change rate at about $t = 20\,\mathrm{s}$.

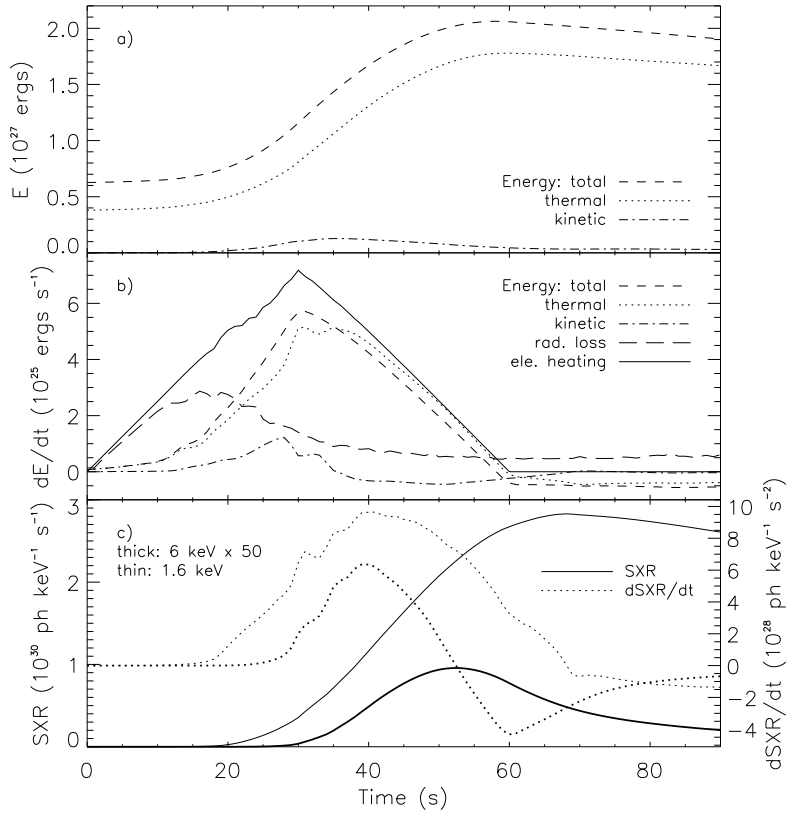

Figure 8.2: History of energy budget and X-ray emission for Case R. (*a*) Spatially integrated total energy (U), thermal energy ($U_{\rm th}$), and kinetic energy (U_k) of the whole loop. (*b*) Time derivative ($\dot{U}$, $\dot{U}_{\rm th}$, and $\dot{U}_k$) of the above three energies (same line styles), together with the total electron energy deposition power ($\dot{\mathcal{E}}_e$, *solid*) and the radiative loss power (L_{rad}, *long dashed*). (*c*) SXR fluxes ($I_{\rm SXR}$, *solid*) at photon energy of 1.6 (*thin*) and 6 keV (*thick*) and their time derivatives ($\dot{I}_{\rm SXR}$, *dotted*). The 6 keV light curve is rescaled up by a factor of 50.

The energy partition between the thermal and kinetic energy also evolves with time. Early in the flare, because evaporation is still in its infancy, the kinetic energy of the system is very small, and the total energy change is dominated by the variation of the thermal energy (Figs. 8.2*a* and 8.2*b*). For example, at $t = 10\,\mathrm{s}$, the kinetic energy is only $8.35 \times 10^{23}\,\mathrm{ergs}$ changing at a rate of $1.91 \times 10^{23}\,\mathrm{ergs\,s^{-1}}$, compared with the values of the

thermal energy: $U_{\rm th} = 3.99 \times 10^{26}$ ergs and $\dot{U}_{\rm th} = 3.50 \times 10^{24}\,{\rm ergs\,s^{-1}}$. As evaporation grows, the kinetic energy rises gradually, which makes the thermal energy deviates from the total energy curve at about $t = 15\,{\rm s}$. The kinetic energy change rate reaches its maximum at $t = 28\,{\rm s}$ just before the evaporation front arrives at the loop apex. Afterwards, $\dot{U}_k$ decreases quickly because of the reflection of the evaporation front and part of the kinetic energy is converted into the thermal energy due to local gas compression at the apex, which leads to the rapid rise of the $\dot{U}_{\rm th}$ curve (Fig. 8.2*b*), although there is no sudden change in the electron energy deposition at this time. This means that, on top of the electron beam heating, gas dynamics can also change energy partition and thus can modulate the thermal energy which would be manifested in the change of the SXR flux (see below). (This would produce further deviation from the Neupert effect.)

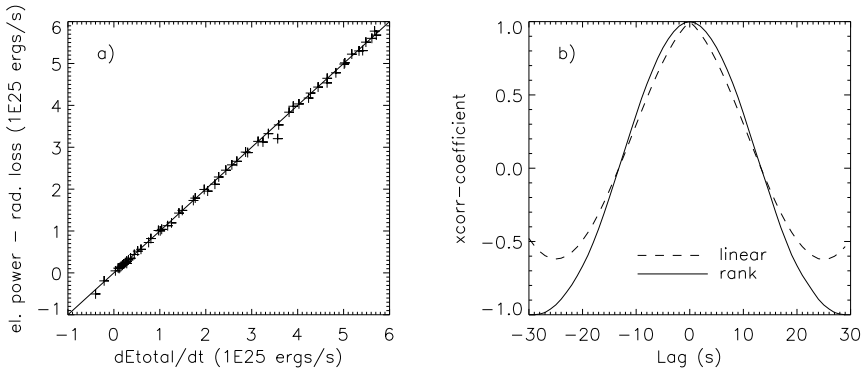

Figure 8.3: Consistency test of eq. (8.4) for Case R. (*a*) The electron energy deposition power minus the radiative loss ($\dot{\mathcal{E}}_e - L_{rad}$) vs. the total energy change rate ($\dot{U}$). The diagonal line corresponds to a perfect agreement. (*b*) Pearson linear (dashed) and Spearman rank (solid) cross-correlation coefficients of the two quantities shown in (*a*), plotted as a function of the time lag. The two coefficients have their maxima of 0.99950 and 0.99956, respectively, at the zero lag.

It is necessary to see if **energy gain and loss** is actually balanced as a consistency check of the code. In Figure 8.3*a* we plot the net energy input ($\dot{\mathcal{E}}_e - L_{\rm rad}$) vs. the total energy change rate ($\dot{U}$). Clearly, the two quantities are almost in perfect agreement. We also cross-correlate the two and the Pearson linear (*dashed*) and Spearman rank[3] (*solid*) cross-correlation coefficients (Fig. 8.3*b*) have a peak value of 0.99950 and 0.99956, respectively, indicating a very high correlation. Therefore we are assured that energy is conserved and equation (8.4) is indeed satisfied in our simulations. We note that this correlation is actually the "real" Neupert effect on the basis of an exact energy budget argument and we will use it as a reference point in this study.

8.2.2 Neupert Effect Test

Let us now check if the Neupert effect is present. We plot in Figure 8.2*c* the spatially integrated thermal SXR photon flux $I_{\rm SXR}$ (*solid*, photons ${\rm keV^{-1}\,s^{-1}}$, at the Sun) at two energies, 1.6 keV (*thin*) and 6 keV (*thin*, scaled by a factor of 50). We find the lower energy

[3]The Spearman rank correlation coefficient is an indicator of an either linear or nonlinear correlation.

SXR light curve rises earlier and faster, and decays later and slower, than the higher energy one. The shape of the 1.6 keV curve resembles that of the thermal energy (8.2*a*) because of their close relationship due to their dependence on n_e and T as noted above. It also mimics commonly observed *GOES* light curves (see, e.g., Fig. 6.1 in Chapter 6). The 6 keV light curve, however, appears comparably short in duration. This is because the 6 keV thermal emission is more sensitive to higher temperature plasmas (peak temperature response at 60 keV) and the temperature dependence of the thermal bremsstrahlung emissivity is very sharp in its rise portion (see Fig. 8.1). Therefore, early in the flare, when high temperature emission measure is small, there is very little 6 keV thermal emission; similarly in the decay phase, the 6 keV emission decreases quickly when the plasma cools off.

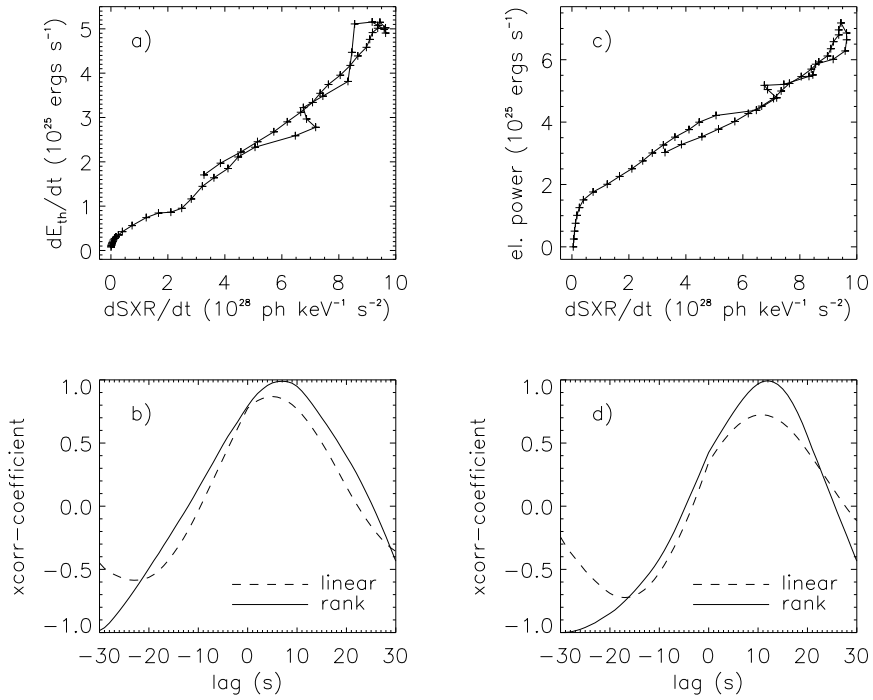

Figure 8.4: Neupert effect test for Case R. (*a*) Thermal energy change rate $\dot{U}_{\rm th}$ vs. SXR derivative $\dot{I}_{\rm SXR}$ (at photon energy of $\epsilon = 1.6\,{\rm keV}$) during the first 60 s of the flare. The solid line that connects the symbols indicates the time evolution, starting near the lower-left corner at $t = 0\,{\rm s}$. $\dot{I}_{\rm SXR}$ has been shifted back in time by 7 s to compensate its delay, as indicated by the cross-correlation analysis (see below and text). (*b*) Pearson linear (dashed) and Spearman rank (solid) cross-correlation coefficients of the two quantities shown in (*a*), plotted as a function of the time lag (> 0 means delay) of $\dot{I}_{\rm SXR}$ relative to $\dot{U}_{\rm th}$. The rank correlation coefficient reaches its maximum value of 0.989 at a lag of 7 s. (*c*) and (*d*) same as (*a*) and (*b*), respectively, but for the correlation between $\dot{\mathcal{E}}_e$ (electron energy deposition power) and $\dot{I}_{\rm SXR}$ (shifted back by 12 s).

To get more detailed timing information, we took the time derivatives of the two SXR fluxes, following the common practice for Neupert effect studies. The result is shown as the dotted lines (*thin*: 1.6 keV, *thick*: 6 keV) in Figure 8.2*c*. By visual comparison with the electron energy deposition power ($\dot{\mathcal{E}}_e$) and the thermal energy change rate ($\dot{U}_{\rm th}$) in

Figure 8.2*b*, we find that these curves resemble each other in one way or another. They all roughly show a triangular shape. Particularly, the $\dot{I}_{\rm SXR}$ curves even follow $\dot{U}_{\rm th}$ in some detail. For example, $\dot{I}_{\rm SXR}$ at both energies exhibits a rapid rise at about $t = 29\,{\rm s}$ when an abrupt increase in $\dot{U}_{\rm th}$ occurs (due to gas dynamics, see above). However, such a detailed change is not present in the $\dot{\mathcal{E}}_e$ curve, which is equivalent to the HXR flux here[4]. Therefore, if one attempts to look for the Neupert effect by comparing the SXR derivative and the HXR flux (as people usually do), such a subtle correlation could be missing in HXRs. In this sense, a more physical Neupert effect would be the relationship between the thermal energy change rate and the SXR derivative.

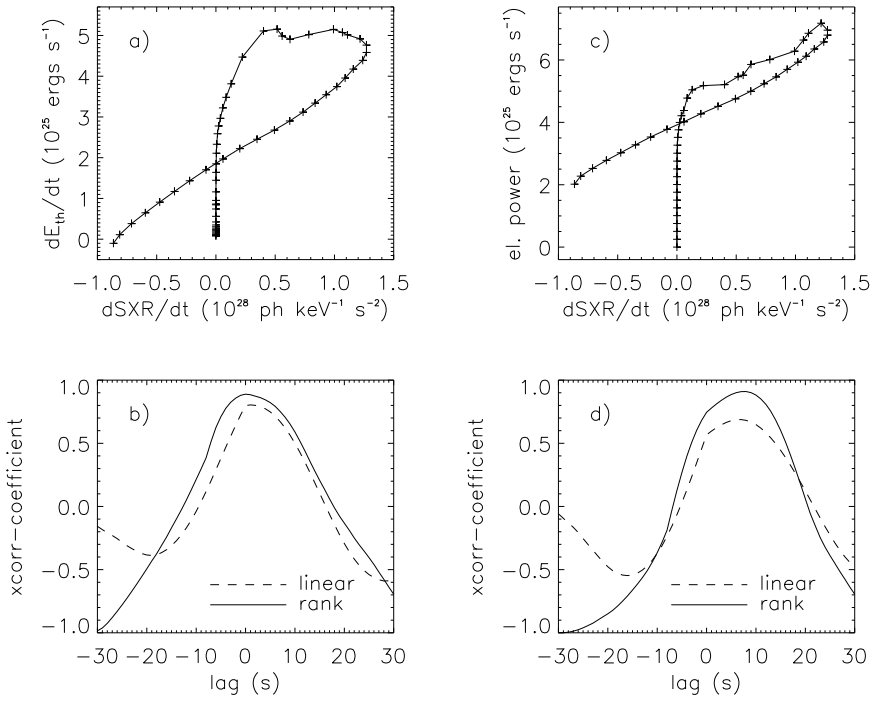

Figure 8.5: Same as Fig. 8.4 (Case R), but for photon energy $\epsilon = 6\,{\rm keV}$. $\dot{I}_{\rm SXR}$ in (*c*) is shifted back by 8 s to compensate its delay.

We have carried out statistical analysis and checked the correlations between these various variables more quantitatively. We first cross-correlated the SXR derivative $\dot{I}_{\rm SXR}$ at 1.6 keV with the thermal energy change rate $\dot{U}_{\rm th}$ and with the electron energy deposition power $\dot{\mathcal{E}}_e$, the correlation coefficients of which are shown in Figures 8.4*b* and 8.4*d*, respectively. For $\dot{I}_{\rm SXR}$ and $\dot{U}_{\rm th}$, the linear correlation coefficient has a peak value of 0.868 at a lag of 5 s, and the rank correlation peaks (max = 0.989) at a lag of 7 s, both indicating a significant correlation and a delay of $\dot{I}_{\rm SXR}$ relative to $\dot{U}_{\rm th}$. Such a delay is also visible in

[4]For Case R only, the HXR flux could not be readily calculated without running the transport and radiation code for the assumed power-law electron spectrum. Here, we use $\dot{\mathcal{E}}_e$ as a protocol for the HXR flux since they are proportional to each other (because the electron spectrum remains constant in time and the bremsstrahlung yield is thus a constant as well).

Figures 8.3*b* and 8.3*c*, say, by comparing the rise portion and the peak position of the corresponding curves. Since their physical relationship is nonlinear *per se* as discussed above, we believe the rank correlation can describe the connection between $\dot{I}_{\rm SXR}$ and $\dot{U}_{\rm th}$ more generally than the linear correlation, although the two correlations give us different perspectives when looking at the same phenomenon. We thus use the delay indicated by the rank correlation to shift $\dot{I}_{\rm SXR}$ back in time and plot $\dot{U}_{\rm th}$ vs. $\dot{I}_{\rm SXR}$ in Figure 8.4*a*. We find these two quantities indeed have a strong correlation since their data points in the scatter plot very much distribute along a straight line. In contrast, for $\dot{I}_{\rm SXR}$ and $\dot{\mathcal{E}}_e$, the linear (rank) correlation coefficients reaches its maximum of 0.724 (0.993) at a lag of 11 s (12 s). This indicates a weaker linear correlation (although a slightly stronger rank correlation), compared with the correlation for $\dot{I}_{\rm SXR}$ and $\dot{U}_{\rm th}$. It also reveals a longer delay, which could be ascribed to the fact that the rise portion of $\dot{U}_{\rm th}$ itself actually delays relative to the energy deposition rate, $\dot{\mathcal{E}}_e$, (Fig. 8.3*b*) because of the strong radiative loss at early times as noted before.

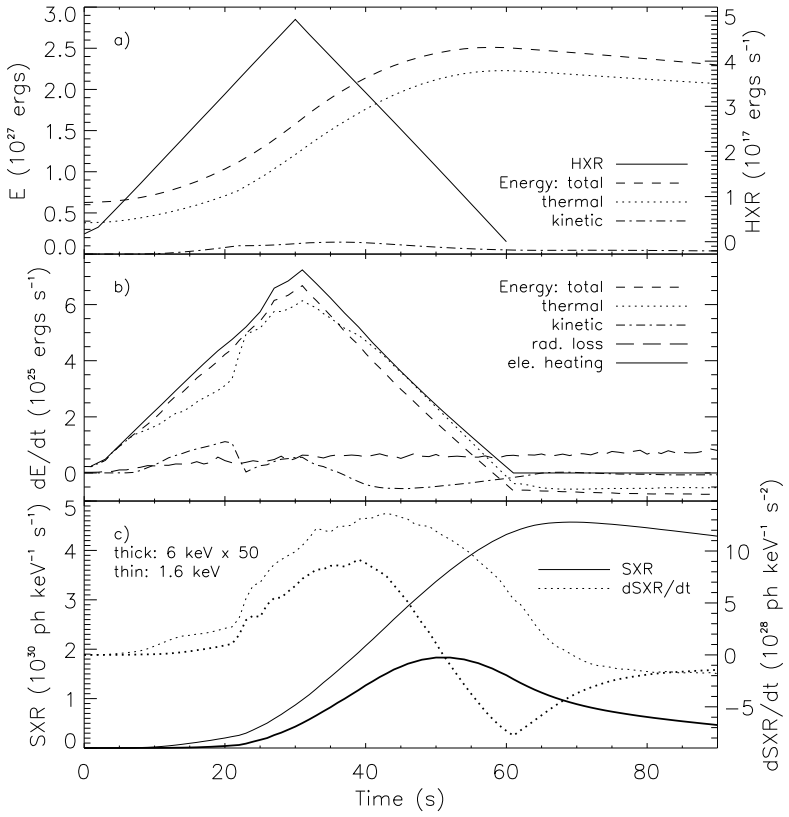

Figure 8.6: Same as Fig. 8.2, but for Case A, with the HXR power of all $\geq$20 keV photons in (*a*).

We also repeated the above analysis for SXR emission at photon energy of 6 keV for comparison. The result is shown in Figure 8.5. In general, we find a weaker correlation and a shorter delay (see Table 8.1). The shorter delay (despite its actual delay in the rise portion) is due to the rapid decrease of the 6 keV light curve during its decay, which mimics

the same trend in the $\dot{\mathcal{E}}_e$ and $\dot{U}_{\rm th}$ curves (Fig. 8.2). However, it is noted that the 1.6 and 6 keV derivatives both peak at about the same time, $t = 40\,$s. As we will show below, this is a particular feature of this Case. It is interesting to see that the curves in Figures 8.5*a* and 8.5*c* both show a crossed loop-like shape, reminiscence of that in Figure 6.12*e*.

8.3 Cases A-D: Combined HD & Particle Calculation

For comparison, we did the same analysis as above for the other four cases, which we describe as follows. The only new quantity is the HXR ($E > 20\,$keV) flux calculated from our radiation code, which we will use here in place of the electron energy deposition power for cross-correlating with the SXR derivative.

8.3.1 Case A: Fiducial Run with SA Model

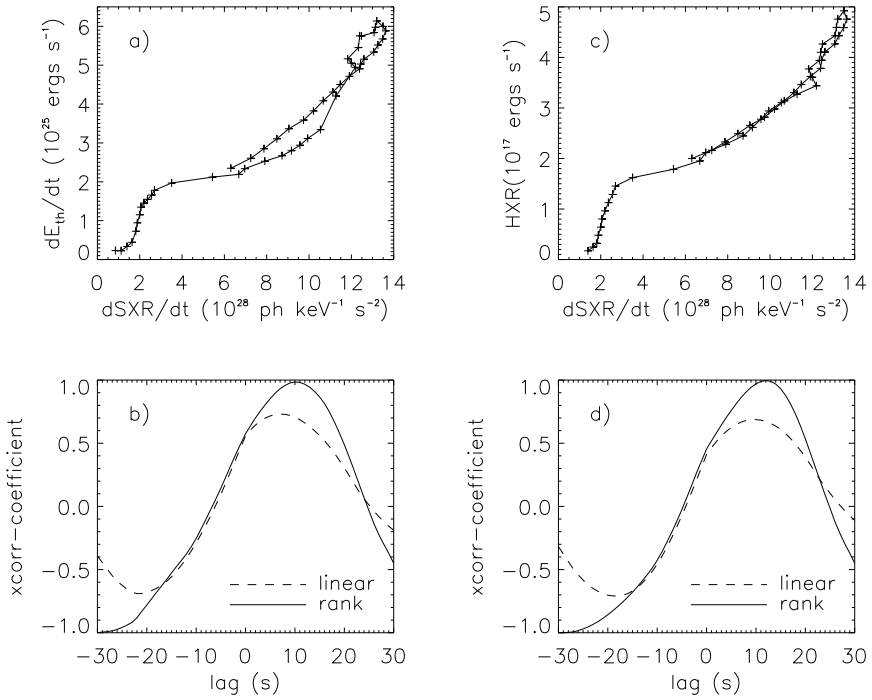

Figure 8.7: Same as Fig. 8.4 but for Case A and the ≥20 keV HXR emission power ($I_{\rm HXR}$) (rather than the electron energy deposition power). SXR derivatives in (*a*) and (*c*) are shifted back in time by 10 and 12 s, respectively, according to their delays indicated by the peak of the Pearson rank correlation coefficient shown in (*b*) and (*d*).

For Case A, the energy budget history is shown in Figure 8.6. We find that the overall evolution of the energies is similar to that of Case R (Fig. 8.6). However, we do see three major differences, the first of which is relatively small importance of the radiative loss here, particularly during the rise phase of the flare. This is because, as we discussed

earlier, the electron spectrum contains a quasi-thermal component at low energies and this produces relatively more energy deposition in the corona than in the upper chromosphere where radiative loss is most efficient. As a result, less energy is available for radiative loss and more energy is left to evaporate the chromospheric plasma. The second difference is that the 6 keV light curve starts its rise earlier than in Case R, because the preferential coronal heating here (vs. more chromospheric heating in Case R) produces relatively higher emission measure at high temperatures from which the 6 keV emission is more productive. The 6 keV light curve also peaks earlier than the 1.6 keV one by about 5 s, as opposed to their concurrence in Case R. For the same reason, we have stronger chromospheric evaporation, and thus higher coronal temperature and density here, resulting in a higher SXR flux with a maximum of 4.57 (vs. 2.83 in Case R) $\times 10^{30}$photons keV^{-1} s^{-1} at 1.6 keV. The third major difference is that Case A has a faster evolution and the evaporation front reaches the loop apex earlier at $t = 22$ s (vs 29 s in Case R). The associated compressional heating produces a sudden jump at this time in the thermal energy change rate, as well as in the two SXR derivative curves.

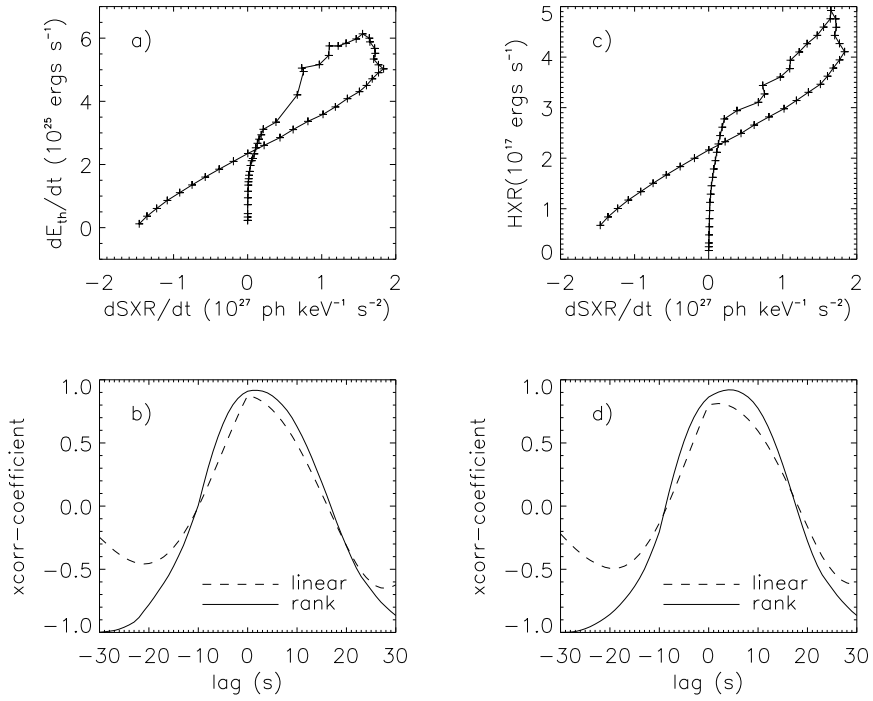

Figure 8.8: Same as Figure 8.7 for Case A but at a photon energy of 6 keV.

We also cross-correlated the SXR derivative with the thermal energy change rate $\dot{U}_{\rm th}$ and the HXR energy flux $I_{\rm HXR}$. The resulting correlation coefficients for the 1.6 keV photon energy are shown in Figure 8.7 We find a weaker linear correlation[5] for both $\dot{U}_{\rm th}$ and

[5]This may have to do with stronger evaporation and more dramatic evolution in this Case, and thus more nonlinear phenomena are invoked.

$I_{\rm HXR}$ with $\dot{I}_{\rm SXR}$, compared with that in Case R (Fig. 8.4), and the peak linear correlation coefficients are 0.731 and 0.687, respectively.

The Pearson rank correlation, however, are very close to that of Case R, and the correlation coefficient for $I_{\rm HXR}$ is even higher (see Fig. 8.7*c* and Table 8.1). This is not surprising, since a linear correlation between these quantities are actually not expected, as we discussed earlier, and their nonlinear correlation seems more likely. In contrast, the correlations for 6 keV photon energy (Fig. 8.8, cf. Fig. 8.5) are somewhat better than those of Case R (see Table 8.1). This might be due to the stronger coronal heating here that favors higher photon energy thermal emission. The shorter (than that in Case R) delay of the 6 keV derivative relative to the HXR flux, which was mentioned above, is also evident from the lag corresponding to the peak (linear or rank) correlation coefficient.

8.3.2 Case B: Variable Electron Spectrum

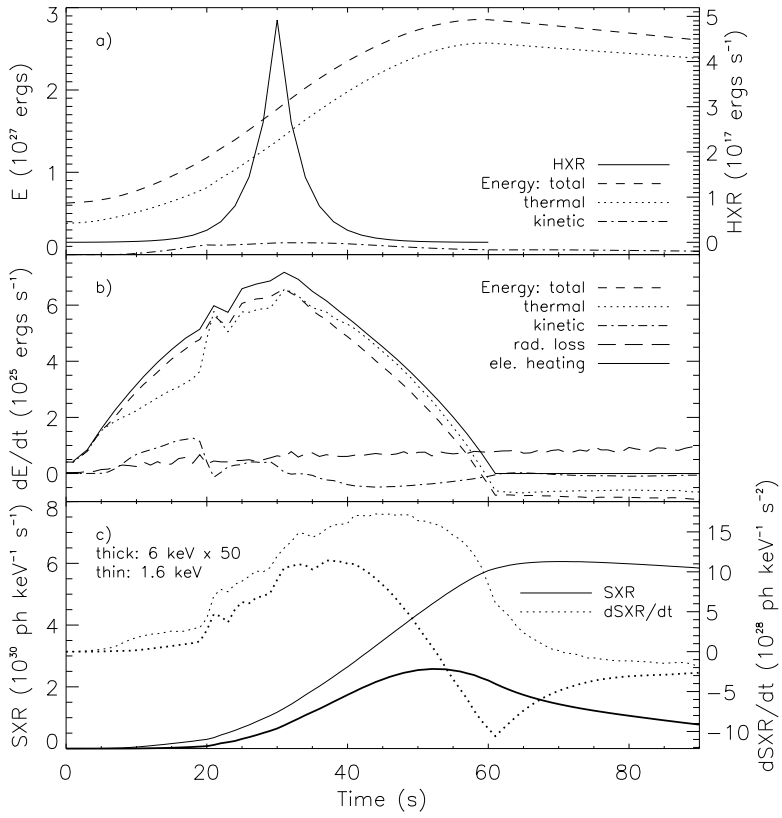

Figure 8.9: Same as Fig. 8.6, but for Case B.

Case B has a particular electron spectrum that experiences a soft-hard-soft variation. The energy budget history is shown in Figure 8.9. Compared with Case A, one of the main differences is the shape of the energy deposition rate, which appears to be warped and slightly higher than the linear one in Case A. This results in somewhat higher heating

rate and faster evaporation (see Table 7.1). Another difference is the shape of the HXR light curve which differs quite a bit from the triangular one in Case A. This is due to the soft-hard-soft variation of the electron spectrum, which modulates the bremsstrahlung yield and thus HXR flux on top of the triangular normalization variation. We also show the cross-correlation result for the 1.6 keV SXR in Figure 8.10. As can be seen, the linear correlation is somewhat weaker than that of Case A, especially for the HXR flux (see Fig. 8.10*c*; note logarithm scale). However, the rank correlation coefficients are similar to that of Case A.

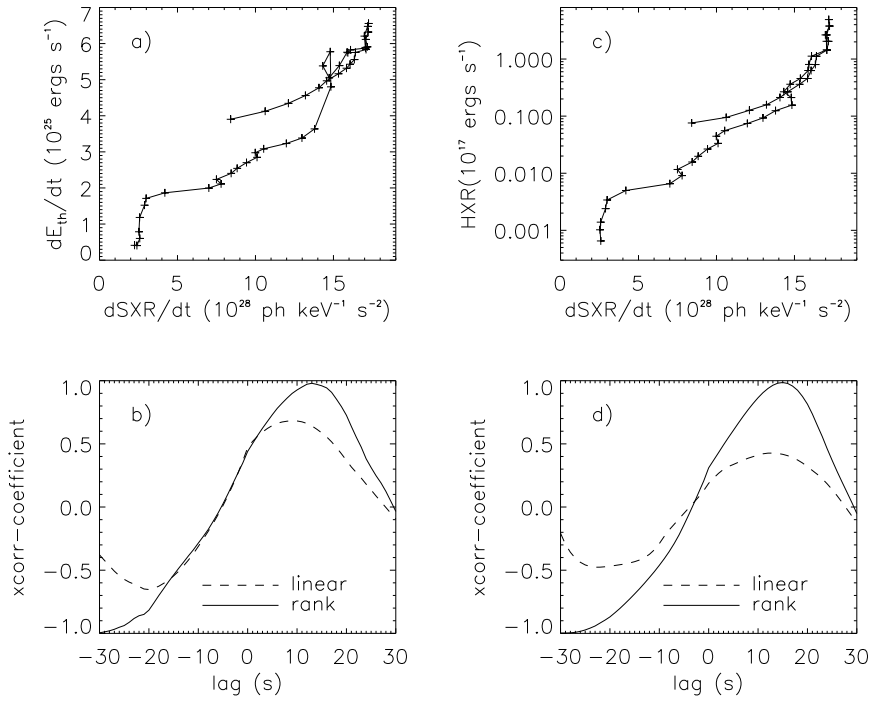

Figure 8.10: Same as Fig. 8.7 but for Case B (at 1.6 keV). SXR derivatives in (*a*) and (*c*) are shifted back by 13 and 15 s, respectively, to account for their delays indicated in (*b*) and (*d*).

8.3.3 Case C: Harder Electron Spectrum

Case C has a harder electron spectrum compared with Case A because of its relatively shorter acceleration timescale ($\tau_p = 100\,\mathrm{s}^{-1}$ vs. $70\,\mathrm{s}^{-1}$). The history of the energy budget (Fig. 8.11) and the cross-correlations (Fig. 8.12) are similar to those of Case A, although its electron spectrum is much harder than that in Case A. The main difference is in the normalization of the HXR flux (see Fig. 8.11*a*) which is about 28 times higher than that of Case A, simply because of harder electron spectrum results in a higher bremsstrahlung yield (see Fig. 6.11) and thus higher HXR emission.

8.3.4 Case D: Smaller Normalization

Case D has an energy input rate 10 times smaller than that of Case A and thus the flare

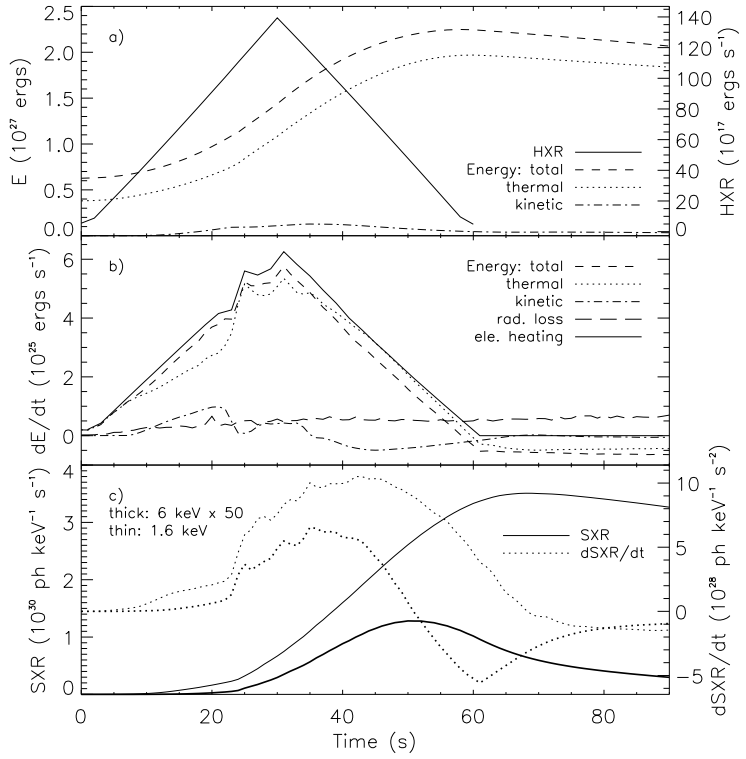

Figure 8.11: Same as Fig. 8.6, but for Case C.

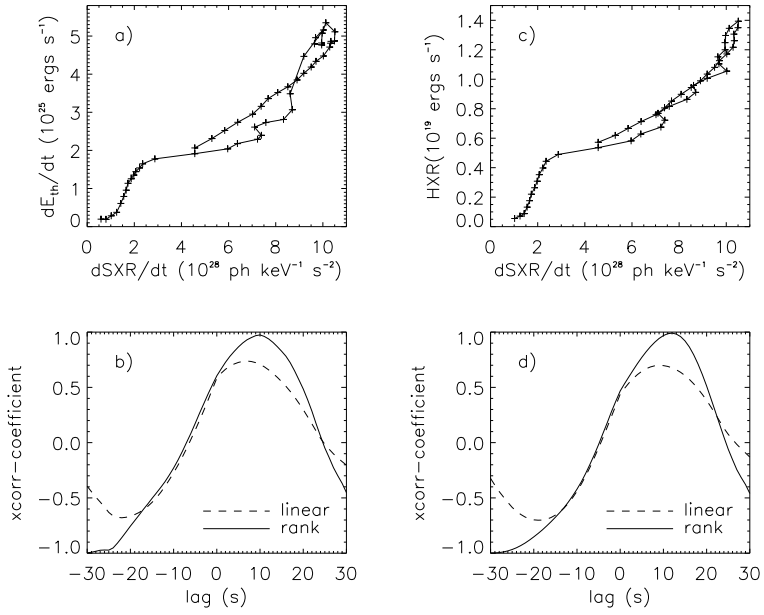

Figure 8.12: Same as Fig. 8.7 but for Case C (at 1.6 keV). SXR derivatives in (*a*) and (*c*) are shifted back by 10 and 12 s, respectively, to make up for their delays.

is weaker by an order of magnitude, as can be seen from the various quantities shown in Figure 8.13. The overall energy evolution appears similar to Cases A-C, except that the evaporation front arrives at the loop apex late ($t = 39\,\mathrm{s}$, well into the decline phase). At this time, the kinetic energy change rate ($\dot{U}_k$) shows the largest continuous drop (with a range of $\Delta\dot{U}_k/\dot{U}_{\max} = 0.33$, normalized by the peak energy input rate $\dot{U}_{\max}$, cf., e.g., 0.16 for Case A) among all the five cases, partly because this drop coincides with the

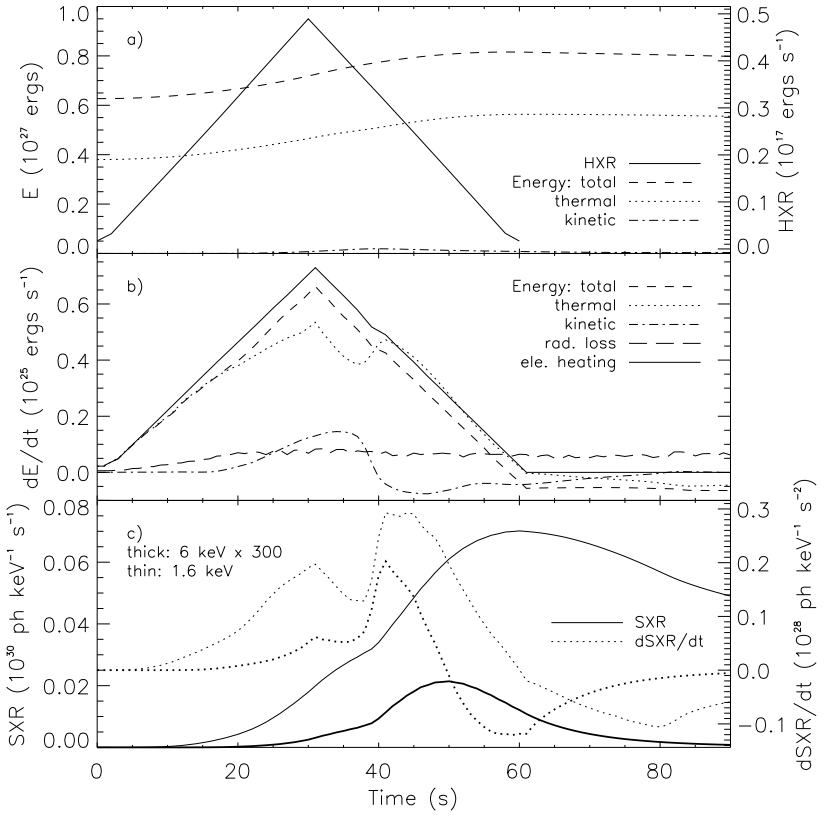

Figure 8.13: Same as Fig. 8.6, but for Case D. Note that the 6 keV SXR light curve in (c) is rescaled by a factor of 300 (cf. 50 in the other four cases) due to the softness of the thermal spectrum in this case of weak evaporation.

decrease of the energy input rate and that of the other cases takes place during the rise phase. In exchange of the decrease in $\dot{U}_k$, the thermal energy change rate still attains a net gain, despite the decrease of the total energy change rate. This rise produces a dramatic increase in SXR flux derivatives at both the 1.6 and 6 keV, which even dwarfs the first peak produced at the time of the maximum total energy input rate. The relative height of the two peaks on the $\dot{U}_{\mathrm{th}}$ curve (Fig. 8.13), however, does the opposite, although the timing of the two peaks agrees with that of the SXR derivative pulses. We attribute this, again, to the nonlinearity of the contribution of density and temperature to thermal bremsstrahlung emission, and particularly to the sensitive dependence on temperature, i.e., the sharp rise

at low temperatures below the maximum of the emissivity curve (see Fig. 8.1). The cross-correlation result is shown in Figure 8.14. Clearly, we find a correlation much weaker the other cases for both the thermal energy change rate and the HXR flux, which can also be seen from the coefficients tallied in Table 8.1.

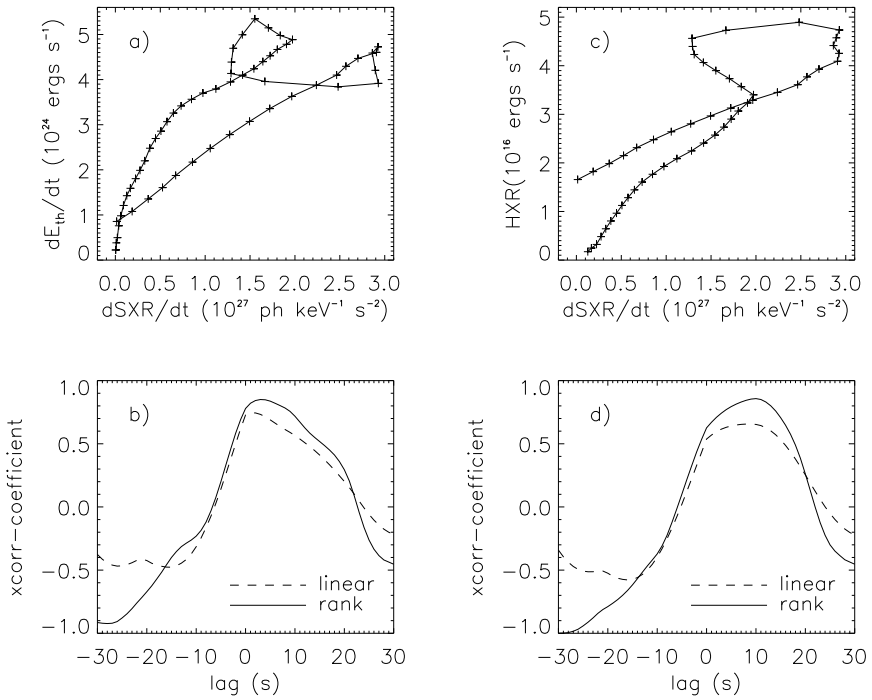

Figure 8.14: Same as Fig. 8.7 but for Case D (at 1.6 keV). SXR derivatives in (*a*) and (*c*) are shifted back by 3 and 10 s, respectively.

8.4 Summary and Discussion

We have performed a test of the Neupert effect for five simulation cases described in Chapter 7, using our SA model and the NRL HD flux tube model. We followed the temporal evolution of various energies (thermal, kinetic, and total), the electron energy deposition power, and the radiative loss, together with thermal and nonthermal bremsstrahlung radiation, spatially integrated over the whole flare volume. We then checked the temporal and statistical correlation between the SXR derivative ($\dot{I}_{\rm SXR}$) and the HXR flux ($I_{\rm HXR}$), and between $\dot{I}_{\rm SXR}$ and the thermal energy change rate ($\dot{U}_{\rm th}$). The statistical correlation analysis for all the five cases is summarized in table 8.1 and we itemize our results as follows.

1. We find that a correlation exists between $\dot{I}_{\rm SXR}$ and $\dot{U}_{\rm th}$, as well as between $\dot{I}_{\rm SXR}$ and $I_{\rm HXR}$. The latter correlation is in agreement with the empirical Neupert effect observed in some (but not all) flares.

Table 8.1: Neupert effect test of simulation cases (ϵ = 1.6, 6 keV).

ϵ	Case	Pearson Linear Correlation				Spearman Rank Correlation			
(keV)		$U_{\rm th}$: coef,	lag (s);	$I_{\rm HXR}$: coef,	lag	$U_{\rm th}$: coef,	lag;	$I_{\rm HXR}$: coef,	lag
1.6	R	0.868	5	0.724	11	0.989	7	0.993	12
	A	0.731	7	0.687	10	0.985	10	0.996	12
	B	0.683	9	0.427	13	0.980	13	0.985	15
	C	0.738	7	0.699	9	0.975	10	0.991	12
	D	0.744	2	0.656	9	0.850	3	0.857	10
6	R	0.804	1	0.688	7	0.889	0	0.909	8
	A	0.876	0	0.812	2	0.916	1	0.920	4
	B	0.890	0	0.624	7	0.923	2	0.933	5
	C	0.875	0	0.815	2	0.907	1	0.910	3
	D	0.696	0	0.589	3	0.854	0	0.833	5

NOTE — For case R, the electron energy deposition rate is used as a protocol for the HXR flux (not available) to calculate the correlation with the SXR derivative.

2. The resulting Spearman rank (linear or nonlinear) correlation coefficients are generally greater than the Pearson (linear) correlation coefficients. When the linear correlation breaks down, the nonlinear correlation still holds (see, e.g., Case B). This is expected since the correlation is essentially nonlinear due to the nonlinearity involved in the radiation (thermal and nonthermal bremsstrahlung) processes.

3. $I_{\rm HXR}$ and $\dot{U}_{\rm th}$ both yield comparable nonlinear correlations with $\dot{I}_{\rm SXR}$, while $\dot{U}_{\rm th}$ is relatively better correlated with $\dot{I}_{\rm SXR}$ linearly.

4. For the rank correlation, the 6 keV SXR has a smaller coefficient in each case than the 1.6 keV one. For the linear correlation, on the other hand, three (Cases A, B, & C) out of the five cases have a stronger correlation in the 1.6 keV category.

5. For the five cases, the cross-correlation analysis indicates that the 1.6 keV SXR derivative is delayed relative to the thermal energy change and the HXR flux. The delay from $I_{\rm HXR}$ is longer than that from $\dot{U}_{\rm th}$ by several seconds, this is because $\dot{U}_{\rm th}$ itself actually lags from $I_{\rm HXR}$ due to the interplay of the energy input and radiative loss, as well as the variation of energy (between thermal and kinetic) partition.

6. The 6 keV SXR exhibits a similar pattern as the 1.6 keV one, but it yields a relatively shorter delay in each category. This is because the 6 keV thermal emission is sensitive to higher temperature plasmas and thus it decays faster as the loop cools, while the 1.6 keV emission lasts longer and then decays more slowly after the impulsive phase.

7. In terms of timing of more subtle features (e.g., spikes in the curves), $\dot{U}_{\rm th}$ generally matches $\dot{I}_{\rm SXR}$, while $I_{\rm HXR}$ does not.

8. In a smaller flare (Case D), all the correlations are much weaker compared with the other flares. This is because a relatively larger fraction of the total energy variation comes from the kinetic energy in this case.

From these findings, we can conclude that, in terms of timing (concurrence and shorter delay) and both linear and nonlinear correlations, the SXR flux is better correlated with

the thermal energy than with the commonly used HXR flux. Many processes, such as gas dynamics, can change the thermal energy in various ways, and signatures of such changes can appear in the SXR radiation, but not in HXRs. This is because thermal SXRs are more directly related to the thermal energy as they are both a function of plasma temperature and density. However, it should be noted that their correlation is not necessarily linear. The reason is that the thermal energy is linearly proportional to n_e and T, while the thermal bremsstrahlung emissivity is a nonlinear function of n_e and T (see eq. [8.7]).

There seems to be a bias for the Neupert effect in the solar physics community that a simple energy argument supports the empirical Neupert effect and a common practice of studying this is to plot the time history of the HXR flux together with the SXR derivative. We point out that a simple linear correlation between $\dot{I}_{\rm SXR}$ and $I_{\rm HXR}$ is not expected, even for purely nonthermal electron heated flare models. As we already noted in Chapter 6, there are several reasons why linearity could break down here. (1) $\dot{I}_{\rm SXR}$ is not proportional to the electron energy input power, but rather closely related (not proportional either) to the thermal energy change rate $\dot{U}_{\rm th}$. (2) The HXR flux is proportional to the electron energy deposition power with a factor of the bremsstrahlung yield, which is not a constant in time but varies with the electron spectrum in a nonlinear way. The energy deposition power also depends on the electron spectrum, but in a different way. (3) The total energy gain is a result of electron energy input power minus radiative loss rate and most of the radiative loss resides in UV and optical (not SXR) wavelengths. (4) The total energy gain is redistributed (partitioned) to different energy forms, i.e., thermal, kinetic, and gravitational energies. Clearly, through this long chain of energy transform, a linear correlation between the SXR derivative and the HXR flux is not expected to be the case. The existence of the Neupert effect in a particular flare supports the purely electron-heating model, but not vice versa. Further deviation from such a correlation will occur when other processes, such as direct heating by turbulence (rather than electrons) is present.